

Electronic Structure of the Metastable Epitaxial Rock-Salt SnSe {111} Topological Crystalline Insulator

Wencan Jin,¹ Suresh Vishwanath,² Jianpeng Liu,³ Lingyuan Kong,⁴ Rui Lou,⁵ Zhongwei Dai,⁶ Jerzy T. Sadowski,⁷ Xinyu Liu,⁸ Huai-Hsun Lien,² Alexander Chaney,² Yimo Han,² Michael Cao,² Junzhang Ma,⁴ Tian Qian,⁴ Shancai Wang,⁵ Malgorzata Dobrowolska,⁸ Jacek Furdyna,⁸ David A. Muller,² Karsten Pohl,⁶ Hong Ding,⁴ Jerry I. Dadap,¹ Huili Grace Xing,^{2,8,*} and Richard M. Osgood, Jr.^{1,†}

¹Columbia University, New York, New York 10027, USA

²Cornell University, Ithaca, New York 14853, USA

³Kavli Institute for Theoretical Physics, University of California, Santa Barbara, California 93106, USA

⁴Beijing National Laboratory for Condensed Matter Physics, and Institute of Physics, Chinese Academy of Sciences, Beijing 100190, China

⁵Department of Physics, Renmin University of China, Beijing 100872, China

⁶University of New Hampshire, Durham, New Hampshire 03824, USA

⁷Center for Functional Nanomaterials, Brookhaven National Laboratory, Upton, New York 11973, USA

⁸University of Notre Dame, Notre Dame, Indiana 46556, USA

(Received 11 October 2016; revised manuscript received 7 August 2017; published 25 October 2017)

Topological crystalline insulators have been recently predicted and observed in rock-salt structure SnSe {111} thin films. Previous studies have suggested that the Se-terminated surface of this thin film with hydrogen passivation has a reduced surface energy and is thus a preferred configuration. In this paper, synchrotron-based angle-resolved photoemission spectroscopy, along with density functional theory calculations, is used to demonstrate that a rock-salt SnSe {111} thin film epitaxially grown on Bi₂Se₃ has a stable Sn-terminated surface. These observations are supported by low-energy electron diffraction (LEED) intensity-voltage measurements and dynamical LEED calculations, which further show that the Sn-terminated SnSe {111} thin film has undergone a surface structural relaxation of the interlayer spacing between the Sn and Se atomic planes. In sharp contrast to the Se-terminated counterpart, the observed Dirac surface state in the Sn-terminated SnSe {111} thin film is shown to yield a high Fermi velocity, 0.50×10^6 m/s, which suggests a potential mechanism of engineering the Dirac surface state of topological materials by tuning the surface configuration.

DOI: 10.1103/PhysRevX.7.041020

Subject Areas: Condensed Matter Physics,
Materials Science,
Topological Insulators

I. INTRODUCTION

Topological phases of matter have attracted much interest from the condensed matter physics community. The initial focus and discovery in this area was on topological insulators (TIs) [1–3], in which time-reversal symmetry gives rise to topologically protected, conducting surface states in insulating bulk crystals. Beyond TIs, the search for new types of topological materials has recently also been extended to other cases, in which the role of topological protection arises from other symmetries, including particle-hole symmetry [4], magnetic translational symmetry [5], and crystalline

symmetry [6]. In the last class of topological materials, topologically nontrivial properties are protected by crystalline symmetry and are thus called topological crystalline insulators (TCIs) [6]. The TCI phase has been theoretically predicted and experimentally verified in narrow-gap IV-VI semiconductors: SnTe [7–11], Pb_{1-x}Sn_xSe [12], and Pb_{1-x}Sn_xTe ($x \geq 0.25$) [13–18], with a rock-salt structure. In these materials, bulk band gaps are located at the four equivalent L points of the face centered cubic Brillouin zone [see Fig. 1(c)]; in addition, the energy-level ordering of the conduction and valence bands at the L points is inverted [19]. A remarkable signature of the TCI phase is the presence of surface states with an even number of gapless Dirac cones on the {001}, {111} surface Brillouin zone (SBZ); these states are protected by the mirror symmetry with respect to the {110} plane [19–21].

For topological materials, in general, the surface configuration is crucial for their Dirac surface states [22,23]. In particular, the tin monochalcogenide TCI is an important platform for investigating the correlation between Dirac

*grace.xing@cornell.edu

†osgood@columbia.edu

Published by the American Physical Society under the terms of the Creative Commons Attribution 4.0 International license. Further distribution of this work must maintain attribution to the author(s) and the published article's title, journal citation, and DOI.

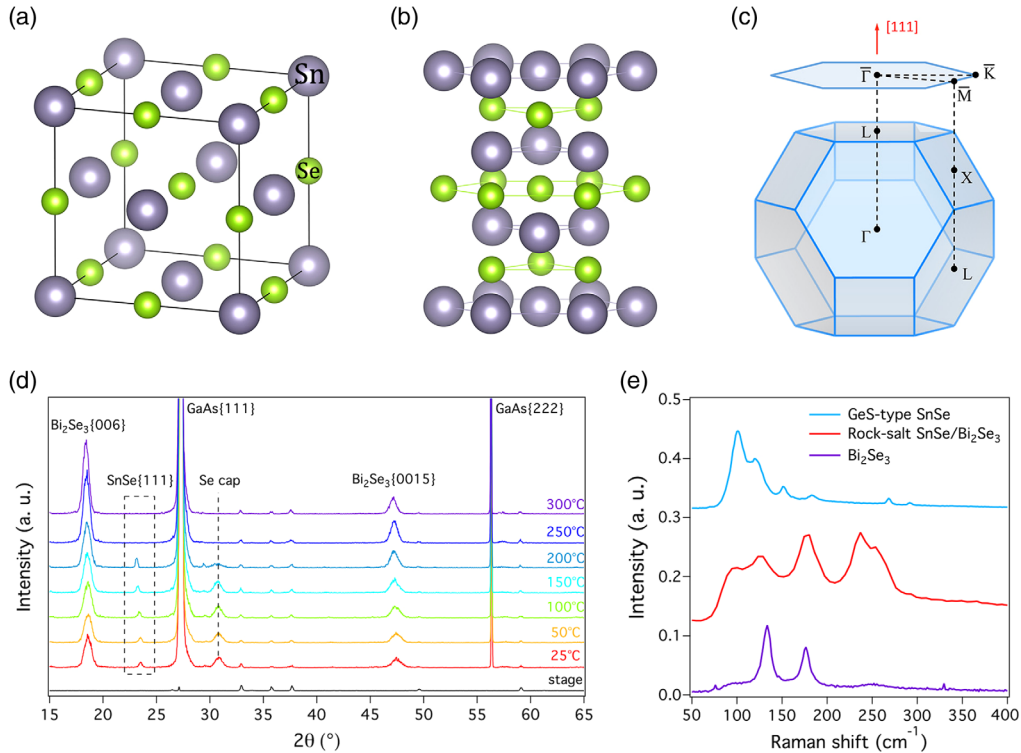


FIG. 1. (a) Schematic of the lattice structure of rock-salt SnSe. (b) Layered rock-salt SnSe depicted along the $\{111\}$ direction. (c) The Brillouin zone of bulk rock-salt SnSe and its projected $\{111\}$ surface Brillouin zone. (d) Temperature-dependent XRD of SnSe/Bi₂Se₃/GaAs acquired using the Cu K_α line. The black dashed box and line denote the diffraction peaks for SnSe $\{111\}$ and Se cap, respectively. (e) Raman spectra of GeS-type SnSe (blue line), rock-salt SnSe (red line), and Bi₂Se₃ (purple line). The excitation wavelength is 488 nm.

surface states and its surface configuration. Since the surface states of TCIs are crystal-symmetry protected, they depend sensitively on the surface orientation. In particular, the $\{001\}$ surface states possess hybridized double Dirac-cones in close vicinity to the \bar{X} point of the $\{001\}$ SBZ, while the $\{111\}$ surface states possess four Dirac cones centered at the $\bar{\Gamma}$ and \bar{M} points of the $\{111\}$ SBZ [8]. In previous experiments, the $\{001\}$ surface states have been more intensively investigated because the $\{001\}$ surface is a natural cleavage plane of rock-salt IV-VI semiconductors. In contrast, the $\{111\}$ surface is a polar surface, which is typically difficult to prepare because of its unstable structure arising from the divergence of the electrostatic energy along the polar direction, i.e., the well-known polar catastrophe [24,25]. This phenomenon may be ameliorated by structural reconfiguration of the surface, which strongly depends on the type of surface termination. Until now, a limited surface termination has been employed in the $\{111\}$ surface of rock-salt TCI. For example, recent studies of $\text{Pb}_{1-x}\text{Sn}_x\text{Te}$ have indicated Te termination of its $\{111\}$ surface [14]. Very recently, the TCI phase in a metastable SnSe $\{111\}$ thin film with rock-salt structure has been observed and was found to be Se terminated and hydrogen passivated using first-principles calculations [26]. Thus, previous experiments have shown the stability of anion-terminated TCIs, either with Te or Se. The

cation-terminated surface, i.e., the truncated-bulk Sn-terminated surface, however, was predicted to be unstable, and, as a result, it undergoes surface reconstruction to diminish its surface energy [27]. Despite its great importance to the full understanding of this family of TCIs and its role in the development of potential high-quality TCI devices, a comprehensive investigation of the correlation between surface configuration and topological surface states has thus far been lacking.

In the present work, we present clear evidence of a stable, truncated-bulk, Sn-terminated, SnSe $\{111\}$ TCI, using a comprehensive battery of experimental and theoretical tests. We also present the first direct evidence of oscillatory structural relaxation of the top atomic layers of this TCI. The surface structure of these thin films is characterized by using selected-area, low-energy, electron diffraction (μ -LEED). In addition, LEED intensity-voltage (I - V) measurements, combined with dynamical LEED calculations, show that our SnSe $\{111\}$ thin films have a Sn-terminated surface without surface reconstruction. Instead, structural relaxation of the interlayer spacing between the Sn and Se atomic planes occurs. Our angle-resolved photoemission spectroscopy measurement demonstrates a robust surface state at the $\bar{\Gamma}$ point, with a Dirac point located about 0.4 eV below E_F . In addition, these measurements reveal a much

higher Fermi velocity (v_F) in the Sn-terminated SnSe than its Se-terminated counterpart. The measured bands of Sn-terminated SnSe $\{111\}$ are accurately reproduced by our first-principles calculations. Despite the fact that most topological material design focuses on composition [28,29], this work paves the way for obtaining a tunable Dirac point and Fermi velocity in TCI by modifying the surface termination; it also clearly shows one potential approach to manipulation of topologically nontrivial surface states by tuning the surface structure through the choice of growth conditions or decapping conditions.

II. RESULTS

A. Characterization

The Sn-Se system is structurally simple, but it contains very rich phases. The energetically stable phase of SnSe has an orthorhombic GeS structure, which is a topologically trivial phase. Molecular beam epitaxy (MBE) is used to grow a SnSe thin film in a rock-salt structure [see Fig. 1(a)]. This film has a thickness of 26 monolayers and is grown on a crystalline Bi_2Se_3 thin film on a GaAs $\{111\}$ substrate. The lattice constant of Bi_2Se_3 is closely matched to the in-plane lattice constant of rock-salt SnSe and, as a result, the epitaxial SnSe $\{111\}$ [see Fig. 1(b)] is constrained to a rock-salt structure. The growth conditions are detailed in the Appendix. The growth was carefully monitored and characterized *in situ* using reflection high-energy electron diffraction (RHEED) (see Ref. [30], Sec. I). The SnSe thin film is protected from ambient atmospheric exposure following growth with a Se cap in the growth chamber. Prior to our microscopy or spectroscopy measurements on each sample, the Se cap was removed by heating at 200 °C for 30 min in ultrahigh vacuum.

The crystalline structure of the epitaxially grown thin film was first investigated using temperature-dependent x-ray diffraction (XRD) from room temperature (RT) to 300 °C (see Ref. [30], Sec. II, for a discussion on off-axis XRD). The results, shown in Fig. 1(d), exhibit consistently well-defined peaks for GaAs $\{111\}$, GaAs $\{222\}$, Bi_2Se_3 $\{006\}$, and Bi_2Se_3 $\{0015\}$. In addition, well-defined peaks for SnSe $\{111\}$ and the Se cap are seen. Note that in both on-axis and off-axis XRD measurements, no peak for the orthorhombic SnSe is observed. Also, the Se cap peaks started to break down at 200 °C, while the SnSe $\{111\}$ peaks slightly shifted because of the thermal expansion and remained intact until 200 °C. This result suggests that heating the sample at 200 °C can successfully remove the Se cap without damaging the SnSe thin film. In addition, ancillary Raman spectra, which are shown in Fig. 1(e), support our supposition that this SnSe layer has a rock-salt structure, which is clearly distinct from the structure of GeS-type SnSe. Finally, note that the well-resolved SnSe and Bi_2Se_3 peaks seen on the as-grown sample indicate no significant intermixing during growth [31].

As mentioned above, there have been no reports of a direct measurement of the surface structure of rock-salt SnSe prior to the present work. Also, since rock-salt SnSe is a metastable phase, we found that transmission electron microscopy, which uses high-energy electron beam bombardment of samples, could trigger a transformation in SnSe and at the SnSe/Se cap interface (see Ref. [30], Sec. III). Similar electron-beam-induced transformation in the Sn-Se system was also reported recently in exfoliated SnSe_2 [32]. In order to establish this surface structure, measurements were carried out on our SnSe thin film using μ -LEED and LEED *I-V*. The resulting SnSe μ -LEED pattern shows one set of sharp hexagonal diffraction spots along with a faint ringlike background. This result is consistent with our thin films having one dominant in-plane crystal orientation along with a small percentage of randomly misaligned small domains. This observation allows us to rule out the (2×1) or $\sqrt{3} \times \sqrt{3}R30^\circ$ reconstruction [27].

Additional measurements were made of the sample surface (see Ref. [30], Secs. IV and V). First, we measure variations in the domains along the surface. The probing electron beam (5 μm in diameter) was translated across the sample for several hundreds of micrometers. No obvious change in the μ -LEED pattern was observed, indicating long-range domain uniformity of the thin film. Second, the surface roughness was quantitatively characterized using variations in the local surface normal (see Ref. [30], Sec. III), and the result indicated that epitaxial SnSe and Bi_2Se_3 layers were remarkably flat. Moreover, in order to enable acquisition of the μ -LEED pattern of GaAs $\{111\}$ substrate, each of the epitaxial thin layers was successively removed *in situ* by heating the sample slowly to 400 °C. The GaAs $\{111\}$ substrate was found to display a well-defined hexagonal diffraction pattern, which was used to provide a known reciprocal lattice template by assuming the known lattice constant of GaAs as 5.65 Å [33]. The in-plane lattice constant of SnSe thin film was then determined to be 4.28 ± 0.03 Å by using the reciprocal vector ratio extracted from our μ -LEED patterns. This value for SnSe is about 1% larger than the published measured value of 4.23 Å [34], yet it is in good agreement with the structural optimized value in density functional theory (DFT) calculations [20,26].

B. Electronic structure

The electronic structure of the SnSe $\{111\}$ sample was directly measured using a synchrotron-based high-resolution ARPES system. Figure 2(a) shows the integrated core-level photoemission spectrum of the sample. Well-defined Se 3*d* and Sn 4*d* spin-orbit doublets are immediately apparent in this figure. The peak at 28 eV is assigned to a replica Sn 4*d* state originating from the chemical shift of the Sn surface. (See Ref. [30], Sec. VI, for a photoionization cross-section analysis.) Note that since 26 layers

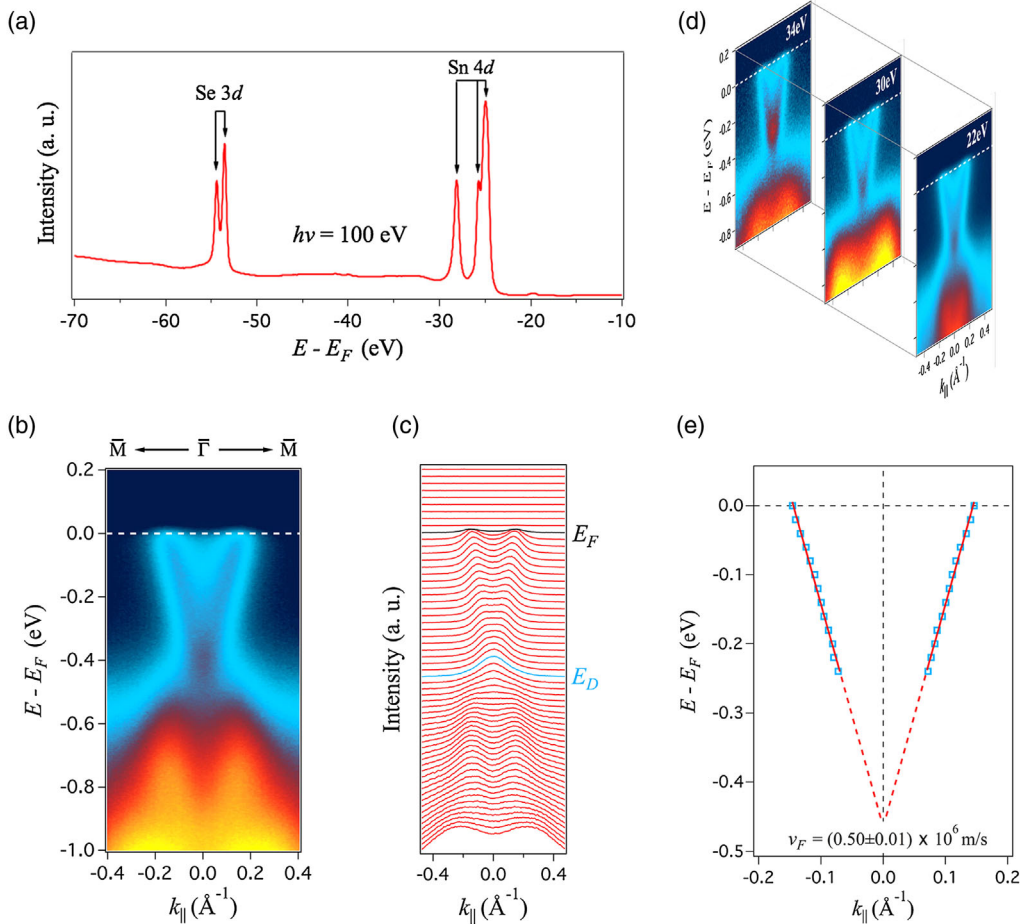


FIG. 2. (a) Core-level photoemission spectrum acquired using 100-eV incident photon energy. (b) ARPES band map ($h\nu = 25$ eV) along the $\bar{M}-\bar{\Gamma}-\bar{M}$ high-symmetry direction. (c) MDC plot of the band dispersion shown in panel (b). Energy positions of the Fermi level and Dirac point are denoted as E_F and E_D , respectively. (d) Excerpts of the photon-energy-dependent ($h\nu = 22, 30$ and 34 eV) ARPES band maps. (e) MDC peak positions (blue dots) and linear fitting (red dashed line).

of SnSe are much thicker than the penetration depth of the low-energy photon, it is unlikely that the surface states of the Bi_2Se_3 buffer layer will be observed. Figure 2(b) shows the ARPES band map along the $\bar{M}-\bar{\Gamma}-\bar{M}$ high-symmetry direction acquired using a 25-eV incident photon energy. Figure 2(c) shows the momentum distribution curves (MDCs) plot of the band map of Fig. 2(b). In sharp contrast to the electronic structure of Se-terminated SnSe with hydrogen passivation, where a Dirac point at the $\bar{\Gamma}$ point is located at approximately 0.1 eV below Fermi level (E_F), we observed Dirac-like linear dispersive bands crossing at about 0.4 eV below E_F . In addition, to verify the k_z ($\{111\}$ direction in BZ) dispersion of the band features, photon-energy-dependent ARPES measurements were carried out (see Ref. [30], Sec. VIII). Figure 2(d) shows the excerpts from the photon-energy-dependent ($h\nu = 22, 30$, and 34 eV) ARPES band map. The Dirac-like band feature does not show any noticeable change with varying incident photon energy over a wide energy range, confirming that it is a surface state. However, the bands with binding energy higher than 0.5 eV do show strongly photon-

energy-dependent evolution, indicating their bulk origin. As shown in Fig. 2(e), linear fitting to the MDC peaks yields a Fermi wave vector of $k_F = 0.14 \pm 0.01 \text{ \AA}^{-1}$ and a high Fermi velocity of $v_F = (0.50 \pm 0.01) \times 10^6 \text{ m/s}$. The Fermi velocity for the Sn-terminated SnSe sample is 3 times larger than for its Se-terminated counterpart.

To aid in interpreting the electronic structure and the topological character of rock-salt SnSe, first-principles calculations were carried out (see the Appendix for calculation details). In contrast to the method reported in Ref. [26], in which dangling bonds were eliminated using hydrogen passivation of the Se termination, a truncated-bulk surface was used in our calculations. In fact, in our calculation, the Sn-terminated surface [see Fig. 3(a)] and the Se-terminated surface [see Fig. 3(b)] are found to yield strikingly different surface states. In the Sn-terminated case, the Dirac point is close to the bulk valence band, while in the Se-terminated case, the Dirac point is close to the bulk conduction band. This result implies that our SnSe $\{111\}$ thin film has a Sn-terminated surface. In fact, a linear fitting to the calculated surface state of the Sn-terminated

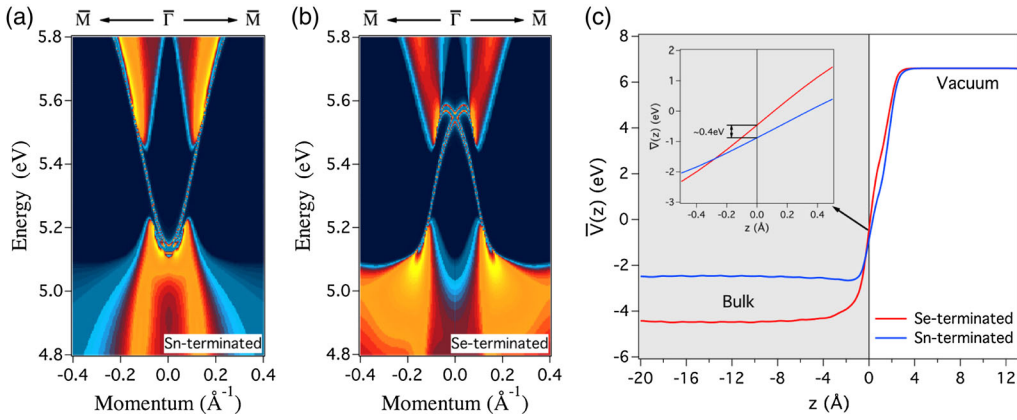


FIG. 3. First-principles calculations of the band structure for (a) Sn-terminated and (b) Se-terminated SnSe {111} thin films. (c) Average electrostatic energy of Sn-terminated (blue) and Se-terminated (red) SnSe thin films as a function of z . The inset shows a magnification of the curves at the surface.

SnSe yields a Fermi velocity of 0.55×10^6 m/s, which is in good agreement with our measured value. The physical origin of the Dirac point shift is attributed to the different electrostatic energy of these two surfaces. In particular, this z -dependent average electrostatic energy is obtained using the formula $\bar{V}(z) = [1/(cA)] \int_{z-c/2}^{z+c/2} dz \int_A dx dy V(x, y, z)$, where $V(x, y, z)$ is the microscopic electrostatic energy, c is the lattice constant in the z direction (z is the normal of the SnSe {111} surface), and A is the area of the unit cell in the x - y plane. The blue (red) curve in Fig. 3(c) is the average electrostatic energy $\bar{V}(z)$ for the Sn-terminated (Se-terminated) slab. Even though $\bar{V}(z)$ for the case of the Se-terminated slab is lower than that of the Sn-terminated slab in the bulk region, the electrostatic energy of the former increases rapidly at the surface. As shown in the inset of Fig. 3(c), at the surface indicated by the vertical gray line, $\bar{V}(z)$ for the case of the Sn-terminated slab is lower than that of the Se-terminated slab by about 0.4 eV; hence, the Sn-terminated case is energetically more favorable than the Se-terminated case. This result is consistent with our ARPES data and first-principles calculations.

C. Surface structure

The surface termination can also be independently confirmed using μ -LEED I - V analysis. Specifically, LEED I - V measurements were carried out to extract the energy dependence of the electron reflectivity of the (00) diffraction beam. Also, I - V curves were calculated using dynamical multiple scattering codes [35] for different trial structures [36]. As a result, the local surface structure can be reliably determined by comparing the experimental reflectivity curve with calculated I - V curves [36–39]. As shown in Fig. 4, the calculated I - V curve of an optimized Sn-terminated surface accurately reproduces the major features of our measured I - V curve, while the calculated I - V curve of a Se-terminated surface is strikingly different from the experimental data. This result further supports the

fact that a SnSe thin film with a Sn-terminated surface can best interpret our data. However, because of the complexity of the surface configuration, alternative interpretations for the surface stability may be possible, such as the presence of random antisite defects without reconstruction; thus, further investigation may be warranted.

An additional important question is the stability of the polar surface of SnSe. As shown in Fig. 1(b), a SnSe {111} thin film has a stacking sequence of Sn^{2+} and Se^{2-} atomic planes, which gives rise to a surface dipole moment and surface charge [24]. Such a stacking sequence can be compensated through the formation of a suitable surface reconstruction [27]; however, such a compensation mechanism has been ruled out in our case through our LEED measurement. Another possible charge-compensation

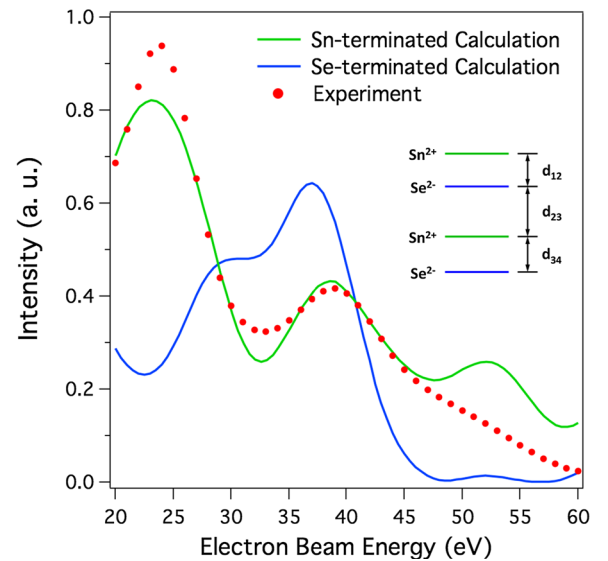


FIG. 4. Calculated LEED I - V curves for the (00) diffraction beam for an optimized Sn-terminated surface (green solid curve) and a Se-terminated surface (blue solid curve) and the measured electron reflectivity curve (red dots).

TABLE I. Calculated optimum top few layer spacings d_{ij} between the i th and j th atomic planes (the inset of Fig. 4) for a SnSe thin film with a Sn-terminated surface and the relative deviation with respect to the bulk layer spacing d_0 .

Parameters	Optimized values (\AA)	$\Delta d_{ij}/d_0$ (%)
d_{12}	1.64	-6.2
d_{23}	1.89	8.1
d_{34}	1.68	-4.1

mechanism is a spatial variation of the slabs along the dipole direction [25]. Therefore, in our structural-optimization procedure, the top four layers of the SnSe {111} thin film with Sn termination are permitted to adjust their interlayer spacing around their initial value of 1.75 \AA , thus enabling charge compensation (see Ref. [30], Sec. X, for a schematic of the charge-compensation mechanism). As a result of this calculation, best-fit parameters are obtained and summarized in Table I, revealing an oscillatory, contraction-expansion-contraction pattern for the structural relaxation in the top few layers of SnSe. This is the first direct evidence of the oscillatory structural relaxation predicted by DFT calculation [27]. Note that a good agreement between calculated and experimental I - V curves is achieved in the energy range of 20–60 eV (electron penetration depth in this range is estimated to be less than 8 \AA), suggesting that the structural relaxation is occurring in the top few layers. However, because of the limited accessible energy range (20–100 eV), a meaningful final R factor was not quantified here.

III. CONCLUSION

In conclusion, we have performed comprehensive experimental and theoretical investigation of the surface and electronic structure of an epitaxial rock-salt SnSe {111} topological crystalline insulator. This investigation allows us to demonstrate that our SnSe {111} thin film has a pristine Sn-terminated surface, which is stabilized via an oscillatory variation of the spacings between the top few layers. In our ARPES experiments, robust surface states with ultrahigh Fermi velocity are observed at the SBZ center. Such distinct properties may lead to potential applications in electronic and spintronic devices, and open a possible route to the manipulation of surface states via tuning of the surface termination in metastable epitaxial topological materials.

ACKNOWLEDGMENTS

The authors acknowledge Liang Fu and David Vanderbilt for very helpful discussions. In addition, we acknowledge Andrew Kummel and Jun Hong Park for the development of the decapping process. The LEEM/LEED research was carried out in part at the Center for Functional Nanomaterials, Brookhaven National Laboratory, and was

supported by the U.S. Department of Energy, Office of Basic Energy Sciences, under Contract No. DE-SC0012704. The MBE growth, Raman, and XRD characterizations were supported by the National Science Foundation (NSF) EFRI-2DARE Project No. 1433490 and NSF Grant No. DMR 1400432. This work also employed the Cornell Center for Materials Research Shared Facilities, which are supported through the NSF MRSEC program (Grant No. DMR-1120296). The DFT calculations were carried out on RUPC. The work of R. M. O., J. D., and W. J. was financially supported by the U.S. Department of Energy under Contract No. DE-FG 02-04-ER-46157. In addition, J. L. was supported by Grants No. DMR-1408838 and No. DMR-1506119. Z. W. D. and K. P. were supported by NSF Grant No. DMR 1006863. R. L. and S. C. W. were supported by the National Natural Science Foundation of China (Grant No. 11274381). L. Y. K., J. Z. M., T. Q., and H. D. were supported by the Ministry of Science and Technology of China (Grants No. 2015CB921300 and No. 2013CB921700), the National Natural Science Foundation of China (Grants No. 11474340 and No. 11234014), and the Chinese Academy of Sciences (Grant No. XDB07000000).

W. J. and S. V. contributed equally to this work.

APPENDIX: MATERIALS AND METHODS

1. Molecular beam epitaxy growth

MBE growth was carried out with n -doped GaAs {111} B substrates using a Riber 32 MBE at the University of Notre Dame. Prior to growth, the substrate was annealed gradually to 700 $^{\circ}\text{C}$ to remove the surface oxide *in situ*. Subsequently, the substrate was exposed to a Se flux of 1.8×10^{-6} Torr at 700 $^{\circ}\text{C}$ for 15 mins. The substrate was then cooled to 340 $^{\circ}\text{C}$ and allowed to stabilize at this latter temperature for 40 mins. Bi_2Se_3 was then grown at the substrate temperature of 340 $^{\circ}\text{C}$ for 15 mins under simultaneous incident elemental Bi and Se fluxes of 3.5×10^{-8} Torr and 1.8×10^{-6} Torr, respectively. Based on the known flux, the expected thickness of the Bi_2Se_3 layer was 12 monolayers (about 12 nm). Subsequent to this step, the substrate temperature was then lowered to 200 $^{\circ}\text{C}$ and stabilized for 30 mins. SnSe growth was done at a substrate temperature of 200 $^{\circ}\text{C}$ for 17 mins under simultaneous incidence of an elemental Sn and a Se flux of 2.1×10^{-8} Torr and 2.4×10^{-8} Torr, respectively. The thickness of SnSe is about 26 monolayers. Se layers were used to cap the as-grown SnSe thin film *in situ* so as to protect the surface from ambient exposure during transport of the sample [31,40,41].

2. X-ray diffraction

Temperature-dependent XRD was done using a Rigaku SmartLab x-ray diffractometer. The Se-capped sample was used for the measurement. The sample stage was made of

AlN, and the measurement was done in an inert atmosphere of nitrogen. The temperature was raised at a rate of 5°C/min and held at the measurement temperature for 10 mins to stabilize the sample prior to measurement. High-resolution measurements were achieved by using a Ge (022) \times 4 monochromator on the source end of the x ray.

3. Angle-resolved photoemission spectroscopy

ARPES measurements were performed at the Dreamline beamline of the Shanghai Synchrotron Radiation Facility (SSRF) with a Scienta D80 analyzer. The samples were decapped in a preparation chamber at 200°C and then measured at 40 K in a vacuum with a pressure of less than 5×10^{-11} Torr. The ARPES data were collected within 12 hours after decapping, during which no signature of surface degradation was observed. The energy and angular resolutions were set to 15 meV and 0.2°, respectively.

4. Low-energy electron microscopy

Note that μ -LEED measurements were performed at the Center for Functional Nanomaterials, Brookhaven National Laboratory, using an ELMITEC AC-LEEM system. In this system, the sample was annealed *in situ* from 200°C (for SnSe) to 300°C (for Bi₂Se₃), and to 500°C (for GaAs), and we acquired the μ -LEED in real time. The spatial resolution is better than 3 nm in the LEEM mode. The electron-beam spot size in the μ -LEED mode was 5 μ m in diameter.

5. First-principles electronic structure calculation

DFT [42,43] calculations of the bulk SnSe electronic structure were performed using a VASP package [44,45]. The generalized gradient approximation (GGA) [46] was adopted to describe the exchange-correlation potential. Hybrid functional (HSE) was also examined and found to yield comparable results to GGA (see Ref. [30], Sec. IX). The in-plane hexagonal lattice parameter was set as $a = 4.24$ Å, and the height of the repeating unit of the Sn-Se bilayer was set as 3.46 Å. The energy cutoff was set to 400 eV. The Brillouin zone was sampled by a $8 \times 8 \times 3$ k -point mesh. A 48-band tight-binding model was then constructed in the Wannier function basis using a Wannier90 package [47–49], where the Wannier functions were generated by projecting the Bloch functions obtained from DFT calculations above onto the spinor s and p orbitals located at all the Sn and Se sites. Finally, the surface states were calculated in a semi-infinite geometry using the iterative surface Green's function method as reported in Ref. [50].

6. Dynamical LEED calculation

The codes from Adams *et al.* [35], which were developed from the programs of Pendry [51] and Van Hove and Tong [52], were used in the dynamical LEED calculations. The

in-plane lattice constant was set to 4.28 Å, a value determined using our μ -LEED pattern. The Debye temperature for SnSe was set as 210 K. The inner potential of SnSe was set as 10.1 eV. Note that 12 ($L = 11$) phase shifts were used in the calculation.

-
- [1] M. Z. Hasan and C. L. Kane, *Colloquium: Topological Insulators*, *Rev. Mod. Phys.* **82**, 3045 (2010).
 - [2] J. E. Moore, *The Birth of Topological Insulators*, *Nature (London)* **464**, 194 (2010).
 - [3] X.-L. Qi and S.-C. Zhang, *Topological Insulators and Superconductors*, *Rev. Mod. Phys.* **83**, 1057 (2011).
 - [4] A. P. Schnyder, S. Ryu, A. Furusaki, and A. W. Ludwig, *Classification of Topological Insulators and Superconductors in Three Spatial Dimensions*, *Phys. Rev. B* **78**, 195125 (2008).
 - [5] R. S. Mong, A. M. Essin, and J. E. Moore, *Antiferromagnetic Topological Insulators*, *Phys. Rev. B* **81**, 245209 (2010).
 - [6] L. Fu, *Topological Crystalline Insulators*, *Phys. Rev. Lett.* **106**, 106802 (2011).
 - [7] Y. Tanaka, Z. Ren, T. Sato, K. Nakayama, S. Souma, T. Takahashi, K. Segawa, and Y. Ando, *Experimental Realization of a Topological Crystalline Insulator in SnTe*, *Nat. Phys.* **8**, 800 (2012).
 - [8] Y. Tanaka, T. Shoman, K. Nakayama, S. Souma, T. Sato, T. Takahashi, M. Novak, K. Segawa, and Y. Ando, *Two Types of Dirac-Cone Surface States on the (111) Surface of the Topological Crystalline Insulator SnTe*, *Phys. Rev. B* **88**, 235126 (2013).
 - [9] P. Littlewood, B. Mihaila, R. Schulze, D. Safarik, J. Gubernatis, A. Bostwick, E. Rotenberg, C. P. Opeil, T. Durakiewicz, J. Smith *et al.*, *Band Structure of SnTe Studied by Photoemission Spectroscopy*, *Phys. Rev. Lett.* **105**, 086404 (2010).
 - [10] Y. Zhang, Z. Liu, B. Zhou, Y. Kim, L. Yang, H. Ryu, C. Hwang, Y. Chen, Z. Hussain, Z.-X. Shen, and S.-K. Mo, *ARPES Study of the Epitaxially Grown Topological Crystalline Insulator SnTe (111)*, *J. Electron Spectrosc. Relat. Phenom.* **219**, 35 (2017).
 - [11] X. Li, F. Zhang, A. MacDonald *et al.*, *SU(3) Quantum Hall Ferromagnetism in SnTe*, *Phys. Rev. Lett.* **116**, 026803 (2016).
 - [12] C. Polley, P. Dziawa, A. Reszka, A. Szczerbakow, R. Minikayev, J. Domagala, S. Safaei, P. Kacman, R. Buczko, J. Adell *et al.*, *Observation of Topological Crystalline Insulator Surface States on (111)-Oriented Pb_{1-x}Sn_xSe Films*, *Phys. Rev. B* **89**, 075317 (2014).
 - [13] S.-Y. Xu, C. Liu, N. Alidoust, M. Neupane, D. Qian, I. Belopolski, J. Denlinger, Y. Wang, H. Lin, L. Wray *et al.*, *Observation of a Topological Crystalline Insulator Phase and Topological Phase Transition in Pb_{1-x}Sn_xTe*, *Nat. Commun.* **3**, 1192 (2012).
 - [14] C. Yan, J. Liu, Y. Zang, J. Wang, Z. Wang, P. Wang, Z.-D. Zhang, L. Wang, X. Ma, S. Ji *et al.*, *Experimental Observation of Dirac-like Surface States and Topological Phase Transition in Pb_{1-x}Sn_xTe (111) Films*, *Phys. Rev. Lett.* **112**, 186801 (2014).

- [15] Y. Tanaka, T. Sato, K. Nakayama, S. Souma, T. Takahashi, Z. Ren, M. Novak, K. Segawa, and Y. Ando, *Tunability of the k -Space Location of the Dirac Cones in the Topological Crystalline Insulator $\text{Pb}_{1-x}\text{Sn}_x\text{Te}$* , *Phys. Rev. B* **87**, 155105 (2013).
- [16] S. Safaei, P. Kacman, and R. Buczko, *Topological Crystalline Insulator (Pb, Sn)Te: Surface States and Their Spin Polarization*, *Phys. Rev. B* **88**, 045305 (2013).
- [17] A. Gyenis, I. Drozdov, S. Nadj-Perge, O. Jeong, J. Seo, I. Pletikosić, T. Valla, G. D. Gu, and A. Yazdani, *Quasiparticle Interference on the Surface of the Topological Crystalline Insulator $\text{Pb}_{1-x}\text{Sn}_x\text{Se}$* , *Phys. Rev. B* **88**, 125414 (2013).
- [18] P. Dziawa, B. Kowalski, K. Dybko, R. Buczko, A. Szczerbakow, M. Szot, E. Łusakowska, T. Balasubramanian, B. M. Wojek, M. Berntsen *et al.*, *Topological Crystalline Insulator States in $\text{Pb}_{1-x}\text{Sn}_x\text{Se}$* , *Nat. Mater.* **11**, 1023 (2012).
- [19] T. H. Hsieh, H. Lin, J. Liu, W. Duan, A. Bansil, and L. Fu, *Topological Crystalline Insulators in the SnTe Material Class*, *Nat. Commun.* **3**, 982 (2012).
- [20] Y. Sun, Z. Zhong, T. Shirakawa, C. Franchini, D. Li, Y. Li, S. Yunoki, and X.-Q. Chen, *Rocksalt SnS and SnSe: Native Topological Crystalline Insulators*, *Phys. Rev. B* **88**, 235122 (2013).
- [21] J. Liu, W. Duan, and L. Fu, *Two Types of Surface States in Topological Crystalline Insulators*, *Phys. Rev. B* **88**, 241303 (2013).
- [22] X. Wang and T.-C. Chiang, *Topological States in Bi_2Se_3 Surfaces Created by Cleavage within a Quintuple Layer: Analysis in Terms of the Shockley Criterion*, *Phys. Rev. B* **89**, 125109 (2014).
- [23] Y. Shi, M. Wu, F. Zhang, and J. Feng, *(111) Surface States of SnTe*, *Phys. Rev. B* **90**, 235114 (2014).
- [24] P. Tasker, *The Stability of Ionic Crystal Surfaces*, *J. Phys. C* **12**, 4977 (1979).
- [25] C. Noguera, *Polar Oxide Surfaces*, *J. Phys. Condens. Matter* **12**, R367 (2000).
- [26] Z. Wang, J. Wang, Y. Zang, Q. Zhang, J.-A. Shi, T. Jiang, Y. Gong, C.-L. Song, S.-H. Ji, L.-L. Wang *et al.*, *Molecular Beam Epitaxy-Grown SnSe in the Rock-Salt Structure: An Artificial Topological Crystalline Insulator Material*, *Adv. Mater.* **27**, 4150 (2015).
- [27] J. Wang, J. Liu, Y. Xu, J. Wu, B.-L. Gu, and W. Duan, *Structural Stability and Topological Surface States of the SnTe (111) Surface*, *Phys. Rev. B* **89**, 125308 (2014).
- [28] C. Polley, V. Jovic, T.-Y. Su, M. Saghier, D. Newby Jr., B. Kowalski, R. Jakiela, A. Barcz, M. Guzewicz, T. Balasubramanian *et al.*, *Observation of Surface States on Heavily Indium-Doped SnTe (111), A Superconducting Topological Crystalline Insulator*, *Phys. Rev. B* **93**, 075132 (2016).
- [29] R. Lou, Z. Liu, W. Jin, H. Wang, Z. Han, K. Liu, X. Wang, T. Qian, Y. Kushnirenko, S.-W. Cheong *et al.*, *Sudden Gap Closure Across the Topological Phase Transition in $\text{Bi}_{2-x}\text{In}_x\text{Se}_3$* , *Phys. Rev. B* **92**, 115150 (2015).
- [30] See Supplemental Material at <http://link.aps.org/supplemental/10.1103/PhysRevX.7.041020> for additional sample characterization and detailed data analysis.
- [31] S. Vishwanath, X. Liu, S. Rouvimov, L. Basile, N. Lu, A. Azcatl, K. Magno, R. M. Wallace, M. Kim, J.-C. Idrobo *et al.*, *Controllable Growth of Layered Selenide and Telluride Heterostructures and Superlattices Using Molecular Beam Epitaxy*, *J. Mater. Res.* **31**, 900 (2016).
- [32] E. Sutter, Y. Huang, H.-P. Komsa, M. Ghorbani-Asl, A. V. Krasheninnikov, and P. Sutter, *Electron-Beam Induced Transformations of Layered Tin Dichalcogenides*, *Nano Lett.* **16**, 4410 (2016).
- [33] M. Kaminska, Z. Liliental-Weber, E. Weber, T. George, J. Kortright, F. Smith, B.-Y. Tsaur, and A. Calawa, *Structural Properties of As-Rich GaAs Grown by Molecular Beam Epitaxy at Low Temperatures*, *Appl. Phys. Lett.* **54**, 1881 (1989).
- [34] A. Mariano and K. Chopra, *Polymorphism in Some IV-VI Compounds Induced by High Pressure and Thin-Film Epitaxial Growth*, *Appl. Phys. Lett.* **10**, 282 (1967).
- [35] D. L. Adams, *A Simple and Effective Procedure for the Refinement of Surface Structure in LEED*, *Surf. Sci.* **519**, 157 (2002).
- [36] J. Sun, J. B. Hannon, R. M. Tromp, P. Johari, A. A. Bol, V. B. Shenoy, and K. Pohl, *Spatially-Resolved Structure and Electronic Properties of Graphene on Polycrystalline Ni*, *ACS Nano* **4**, 7073 (2010).
- [37] J. Hannon, J. Sun, K. Pohl, and G. Kellogg, *Origins of Nanoscale Heterogeneity in Ultrathin Films*, *Phys. Rev. Lett.* **96**, 246103 (2006).
- [38] J. Sun, J. Hannon, G. Kellogg, and K. Pohl, *Local Structural and Compositional Determination via Electron Scattering: Heterogeneous Cu (001)-Pd Surface Alloy*, *Phys. Rev. B* **76**, 205414 (2007).
- [39] Z. Dai, W. Jin, M. Grady, J. T. Sadowski, J. I. Dadap, R. M. Osgood, and K. Pohl, *Surface Structure of Bulk 2H-MoS₂ (0001) and Exfoliated Suspended Monolayer MoS₂: A Selected Area Low Energy Electron Diffraction Study*, *Surf. Sci.* **660**, 16 (2017).
- [40] S. Vishwanath, X. Liu, S. Rouvimov, P. C. Mende, A. Azcatl, S. McDonnell, R. M. Wallace, R. M. Feenstra, J. K. Furdyna, D. Jena *et al.*, *Comprehensive Structural and Optical Characterization of MBE Grown MoSe₂ on Graphite, CaF₂ and Graphene*, *2D Mater.* **2**, 024007 (2015).
- [41] J. H. Park, S. Vishwanath, X. Liu, H. Zhou, S. M. Eichfeld, S. K. Fullerton-Shirey, J. A. Robinson, R. M. Feenstra, J. Furdyna, D. Jena *et al.*, *Scanning Tunneling Microscopy and Spectroscopy of Air Exposure Effects on Molecular Beam Epitaxy Grown WSe₂ Monolayers and Bilayers*, *ACS Nano* **10**, 4258 (2016).
- [42] P. Hohenberg and W. Kohn, *Inhomogeneous Electron Gas*, *Phys. Rev.* **136**, B864 (1964).
- [43] W. Kohn and L. J. Sham, *Self-Consistent Equations Including Exchange and Correlation Effects*, *Phys. Rev.* **140**, A1133 (1965).
- [44] G. Kresse and J. Furthmüller, *Efficient Iterative Schemes for Ab Initio Total-Energy Calculations Using a Plane-Wave Basis Set*, *Phys. Rev. B* **54**, 11169 (1996).
- [45] G. Kresse and J. Furthmüller, *Efficiency of Ab-Initio Total Energy Calculations for Metals and Semiconductors Using a Plane-Wave Basis Set*, *Comput. Mater. Sci.* **6**, 15 (1996).

- [46] J.P. Perdew, K. Burke, and M. Ernzerhof, *Generalized Gradient Approximation Made Simple*, *Phys. Rev. Lett.* **77**, 3865 (1996).
- [47] N. Marzari and D. Vanderbilt, *Maximally Localized Generalized Wannier Functions for Composite Energy Bands*, *Phys. Rev. B* **56**, 12847 (1997).
- [48] I. Souza, N. Marzari, and D. Vanderbilt, *Maximally Localized Wannier Functions for Entangled Energy Bands*, *Phys. Rev. B* **65**, 035109 (2001).
- [49] A.A. Mostofi, J.R. Yates, Y.-S. Lee, I. Souza, D. Vanderbilt, and N. Marzari, *Wannier90: A Tool for Obtaining Maximally-Localised Wannier Functions*, *Comput. Phys. Commun.* **178**, 685 (2008).
- [50] M.L. Sancho, J.L. Sancho, J.L. Sancho, and J. Rubio, *Highly Convergent Schemes for the Calculation of Bulk and Surface Green Functions*, *J. Phys. F* **15**, 851 (1985).
- [51] J. Pendry and G.P. Alldredge, *Low Energy Electron Diffraction: The Theory and Its Application to Determination of Surface Structure*, *Phys. Today* **30**, No. 2, 57 (1977).
- [52] M. A. Van Hove and S. Y. Tong, *Surface Crystallography by LEED: Theory, Computation and Structural Results*, Vol. 2 (Springer Science & Business Media, New York, 2012).